Subtissue Thermal Sensing Based on Neodymium-Doped LaF_3 Nanoparticles

Uéslen Rocha,[†] Carlos Jacinto da Silva,[†] Wagner Ferreira Silva,[†] Ilde Guedes,[‡] Antonio Benayas,[∞] Laura Martínez Maestro,[§] Mónica Acosta Elias,[⊥] Enrico Bovero,[∥] Frank C. J. M. van Veggel,[∥] José Antonio García Solé,[§] and Daniel Jaque[§,*]

[†]Grupo de Fotônica e Fluidos Complexos, Instituto de Física, Universidade Federal de Alagoas, 57072-970 Maceió, Alagoas, Brazil, [‡]Departamento de Física, Universidade Federal do Ceará, Campus do PICI, Caixa Postal 6030, 60455-760 Fortaleza-CE, Brazil, [∞]Institut National de la Recherche Scientifique - Énergie, Matériaux et Télécommunications, Université du Québec, Varennes, QC J3X 1S2, Canada, [§]Fluorescence Imaging Group, Departamento de Física de Materiales C-04, Instituto Nicolás Cabrera, Facultad de Ciencias, Universidad Autónoma de Madrid, 28049 Madrid, Spain, [⊥]Departamento de Física, Universidad de Sonora, Boulevard Luis Encinas y Rosales s/n C.P. 83000, Hermosillo, Sonora, México, and [∥]Department of Chemistry, University of Victoria, Victoria, British Columbia, Canada V8W 3V6

ABSTRACT In this work, we report the multifunctional character of neodymium-doped LaF_3 core/shell nanoparticles. Because of the spectral overlap of the neodymium emission bands with the transparency windows of human tissues, these nanoparticles emerge as relevant subtissue optical probes. For neodymium contents optimizing the luminescence brightness of Nd^{3+}:LaF_3 nanoparticles, subtissue penetration depths of several millimeters have been demonstrated. At the same time, it has been found that the infrared emission bands of Nd^{3+}:LaF_3 nanoparticles show a remarkable thermal sensitivity, so that they can be advantageously used as luminescent nanothermometers for subtissue thermal sensing. This possibility has been demonstrated in this work: Nd^{3+}:LaF_3 nanoparticles have been used to provide optical control over subtissue temperature in a single-beam plasmonic-mediated heating experiment. In this experiment, gold nanorods are used as nanoheaters while thermal reading is performed by the Nd^{3+}:LaF_3 nanoparticles. The possibility of a real single-beam-controlled subtissue hyperthermia process is, therefore, pointed out.

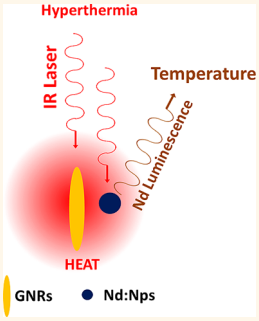

KEYWORDS: nanothermometry · hyperthermia · fluorescence imaging · fluorescence quantum yield · gold nanorods

During the last several years, fluorescence bioimaging has experienced a tremendous development that has pointed out the viability of achieving, in a short time, three-dimensional imaging of biosystems with submicrometric resolution. This is of special relevance for early detection and treatment of diseases as well as for dynamical *in vitro* and *in vivo* studies of a great variety of biosystems.[1−7] This progress has been sustained by the simultaneous advances in experimental techniques (such as ultrafast laser sources for multiphoton imaging and high sensitivity detectors) and in the synthesis of novel biocompatible luminescence probes with outstanding properties.

The constant refinement and optimization of preparation techniques has led to the ability to tailor and predesign the optical and physical properties of luminescent nanoparticles (hereafter NPs) with sizes below a few tens of nanometers and their surfaces. As a consequence, colloidal luminescent NPs have already been used as efficient biolabels in fluorescence imaging of various tissues, small animals, as well as individual cells (including malignant cells).[8−13] Motivated by these encouraging results, many groups around the world have focused their research on the synthesis of novel luminescent NPs. Generally speaking, this research activity has three different battlefronts.

The first one is the synthesis of luminescent nanoparticles with an enhanced brightness, so that high contrast bioimages can be obtained with low excitation intensities (so that light-induced collateral effects in the biosystem under investigation are avoided).

Second, much effort is being done in the synthesis of luminescent nanoparticles working in the infrared region. On one side, NPs emitting and excited in the infrared (in combination with the use of recently elaborated new optical techniques) have already

* Address correspondence to daniel.jaque@uam.es.

Received for review September 20, 2012 and accepted January 11, 2013.

Published online January 12, 2013
10.1021/nn304373q

been proposed for fluorescence bioimaging applications requiring optical penetration into tissues, such as those related to small animal imaging.[14−17] On the other hand, infrared emitting NPs have also been proposed as basic blocks for luminescence activation of chemical reactions in cell treatment (such as the generation of singlet oxygen).[18,19]

The third battlefront and probably the most challenging one is the synthesis of multifunctional luminescent NPs capable of providing additional information of the biosystem under imaging. The working principle of multifunctional luminescent NPs relies on the modifications caused in their luminescence spectra by slight variations in the environment conditions (such as temperature, chemical composition, pH level, density, and so on).[20−22] In this case, an appropriate spectral analysis of the luminescence generated by the nanoparticles provides information about the properties of the biosystem in which these nanoparticles are incorporated. In particular, much attention is being paid to multifunctional luminescent NPs capable of thermal sensing, that is, working as luminescent nanothermometers (NThMs).[23−28] Thermal sensing in biosystems is of extreme interest.[29,30] From a fundamental point of view, a complete understanding of the dynamics of any biosystem (especially at the cellular level) requires an accurate knowledge of its temperature since it affects, for instance, the cell division rate as well as the cell survival rates.[31] High-resolution thermal sensing has also been proposed as a new avenue for early detection of a great variety of diseases and dysfunctions such as cancer and localized inflammations.[32] In the particular case of cancer, the faster metabolism of cancer cells (as compared to normal cells) leads to the appearance of temperature singularities at tumor locations.[33] High sensitivity thermal sensing would allow tumor detection at early stages, in this way increasing the expected success of treatments. Thermal sensing is also required for controlled hyperthermia treatments,[34] where the cancer cells are heated to the cytotoxic level (43−45 °C).[35] Cell heating could directly cause cell death (*via* apoptosis or necrosis) and/or an increment in its susceptibility to subsequent treatments such as radiation or chemotherapy.[36] Hyperthermia treatments have already been found to be applicable in a great variety of cancers (including breast, cervical, lung, prostate, and skin cancers). During hyperthermia treatments, an accurate control over the local temperature increment is required in order to minimize collateral damage in healthy tissues surrounding the hyperthermia target. Due to the subtissue allocation of most tumors into the body, such a thermal reading would require the use of fluorescent NThMs working in the infrared region (within the *biological window*),[37] so that large penetration lengths into the tissues could be obtained. It is possible to find in the literature numerous examples of highly efficient fluorescent NThMs,[23,24] although most of them are not capable of subtissue thermal sensing because their luminescence bands lie in the visible range. Therefore, and due to their practical applications, the pursuit of highly efficient infrared emitting luminescent NThMs is becoming the main task of many research groups.

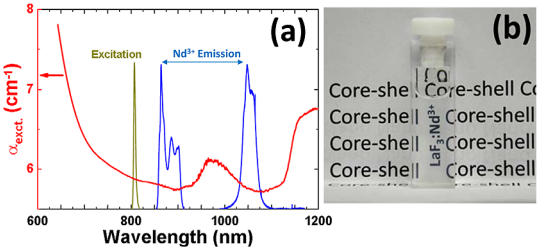

Figure 1. (a) Wavelength dependence of the extinction coefficient of a characteristic phantom tissue (simulating the optical properties of *in vitro* human skin) in the 600−1200 nm spectral range. The emission spectrum of Nd^{3+} ions in LaF_3 nanoparticles is also included. Note that these two emission bands nearly match the minima in the extinction coefficient of the phantom tissue. The spectrum of the 808 nm laser (excitation) source employed all along this work is also included. (b) Photograph of the colloidal solution of Nd^{3+}:LaF_3 nanoparticles used in this work.

In this work, we present to the scientific community the ability of neodymium-doped LaF_3 (core)/undoped LaF_3 (shell) colloidal NPs (hereafter Nd^{3+}:LaF_3 NPs) as subtissue luminescent NThMs. These NPs have been proposed in the past as high-brightness NPs with potential application in bioimaging, with the additional advantage of relatively simple and fast preparation procedures.[38−43] We demonstrate here that these NPs simultaneously show high luminescence quantum yields (QYs) and improved penetration lengths into tissues when compared to other luminescent systems, such as quantum dots. In addition, they present thermal sensitivity by means of thermally induced changes in several emission features. On the basis of this unique combination of properties, we have provided the first demonstration of a single-beam sub-tissue-controlled heating process (subtissue hyperthermia process) based on the combination of Nd^{3+}:LaF_3 NPs and gold nanorods (GNRs) that act as nanothermometers and nanoheaters, respectively.

RESULTS AND DISCUSSION

Figure 1a shows the room temperature emission spectrum of a colloidal solution of Nd^{3+}:LaF_3 NPs (Figure 1b) obtained under 808 nm continuous wave excitation. The presence of the characteristic bands of Nd^{3+} ions at around 900 and 1060 nm (corresponding to the $^4F_{3/2} \rightarrow {}^4I_{9/2}$ and $^4F_{3/2} \rightarrow {}^4I_{11/2}$ transitions, respectively) is evidenced. For the purpose of subtissue imaging and sensing, the spectral position of these two bands is especially favorable. Indeed, they match well the minima that the extinction coefficients of human tissues show within the biological window. In order to illustrate this outstanding property, we have

also included in Figure 1a the extinction coefficient of a phantom tissue that mimics that of an "*in vitro*" human skin tissue.[44] As can be observed, the two characteristic emission bands of Nd^{3+} ions are spectrally allocated at the extinction plateau. In this plateau, the tissue absorption (due to the presence of water and other components such as hemoglobin)[44−47] vanishes in such a way that the extinction coefficient is given basically by the presence of light scattering. The two characteristic neodymium emission bands are, indeed, located at both sides of the characteristic water absorption band centered at 980 nm. Figure 1a also includes the spectrum of the laser radiation used for optimum excitation of the Nd^{3+} emission that, in our experimental conditions, is centered at 808 nm. As can be observed, excitation radiation also lies within the *biological window*.[37] As we will show later in this work, the fact that optimum excitation of Nd^{3+}:LaF_3 NPs is at 808 nm is an interesting advantage. It coincides with the plasmon resonance wavelength of the most efficient gold nanorods used for photothermal therapies.[48]

Data included in Figure 1a suggest large penetration depths into tissues for both excitation and emission radiations, postulating the use of Nd^{3+}:LaF_3NPs for subtissue imaging and sensing. Nevertheless, the achievement of large penetration depths would also require an adequate choice of the neodymium content in order to optimize the luminescence brightness. In neodymium-doped luminescent systems, luminescence brightness is strongly dependent on Nd^{3+} concentration.[49−51] Indeed, the luminescent brightness of Nd^{3+}-doped systems is traditionally evaluated by the $[Nd^{3+}]\cdot\Phi_{lum}$ product, in which $[Nd^{3+}]$ is the neodymium concentration and Φ_{lum} is the emission quantum yield, defined as the fraction of excited Nd^{3+} ions that de-excite through radiative transitions.[52] The term $[Nd^{3+}]$ is directly related to the fraction of incident excitation photons that are absorbed by a single NP. Thus, the $[Nd^{3+}]\cdot\Phi_{lum}$ product is proportional to the fraction of excitation photons that are finally emitted by the NPs; that is, it is a relative indicator of the NP brightness. In general, in Nd^{3+}-doped systems, the presence of both cross-relaxation and energy migration processes between Nd^{3+} ions makes Φ_{lum} decrease with increasing Nd^{3+} concentration. This fact leads to the existence of an optimum neodymium concentration maximizing the luminescence brightness (*i.e.*, to a maximum in the $[Nd]\cdot\Phi_{lum}$ product).[52] The determination of such optimum content requires the accurate and absolute determination of Φ_{lum}. This is not an easy task and requires, for instance, the use of the so-called thermal lens (TL) technique whose fundamentals have been explained elsewhere.[53−55] This technique has already been successfully applied for determining Φ_{lum} of colloidal suspensions of semiconductor quantum dots (QDs).[56,57] Indeed, to the best of our knowledge, this work constitutes the first time that

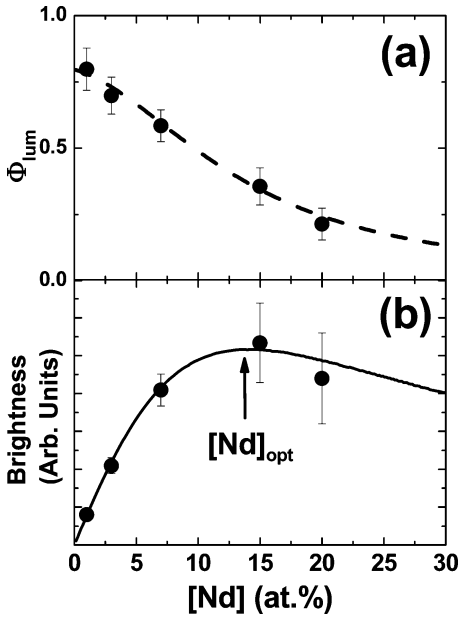

Figure 2. (a) Luminescence quantum efficiency (Φ_{lum}) of Nd^{3+}:LaF_3 nanoparticles as a function of the Nd^{3+} content. Dots are experimental data obtained from thermal lens spectroscopy, and the dashed line is a guide for the eye. (b) Concentration dependence of the brightness as given by the $[Nd^{3+}]\cdot\Phi_{lum}$ product where $[Nd^{3+}]$ is the neodymium content. The existence of an optimum Nd^{3+} content at around 15 atom % (indicated by an arrow) is evidenced.

TL is applied for the determination of the fluorescence quantum yield of rare-earth-doped NPs. Figure 2a shows the experimentally determined room temperature luminescence quantum yield of our Nd^{3+}:LaF_3NPs as a function of the Nd^{3+} content. It is clear from Figure 2a that Φ_{lum} decreases monotonously with the Nd^{3+} concentration. As for other neodymium-doped luminescent systems, this is attributed to the concentration-activated energy migration and cross-relaxation processes that increase the nonradiative decay rate.[58] It should be noted here that the passive LaF_3 shell plays an important role by minimizing the possible quenching of Nd^{3+} fluorescence caused by surface defects that would occur in nonshielded Nd^{3+}:LaF_3 NPs. For low Nd^{3+} concentrations, the luminescence quantum yield is as large as 0.8, whereas it decreases to 0.2 for "moderate" doping levels of 20 atom %. These values can be compared to those previously reported for Nd^{3+}:LaF_3 NPs by other research groups, with them being in reasonable agreement.[59,60] Note that these values of Φ_{lum} can also be compared to those recently reported for CdTe-QDs,[56] whose maximum luminescence quantum yield is close to 0.5 for intermediate sizes (around 4 nm), decreasing to 0.2 for "small" and "large" sizes (close to 1 and 8 nm, respectively). Moreover, it is important to remark here that these yields correspond to visible (one-photon) excitation, which is unpractical for deep tissue penetration experiments, for which two-photon excitation is needed.[61]

Nevertheless, the quantum yield values reported in this work can also be compared to those recently

reported for other similar core/shell nanoparticles: neodymium-doped core/shell $NaGdF_4$ NPs.[17] For the same nominal Nd^{3+} content (3 atom %), the quantum yields of Nd^{3+}:LaF_3 and Nd^{3+}:$NaGdF_4$ NPs are 70 and 40%, respectively. Indeed, this fact suggests that the Nd^{3+}:LaF_3 NPs under study in this work emerge as high-brightness fluorescent NPs. However, it should be noted that the remarkable difference observed between the quantum yields of Nd^{3+}:LaF_3 and Nd^{3+}:$NaGdF_4$ NPs could also be influenced by the fact that they were determined by using different experimental procedures (in this work, we used the thermal lens spectroscopy, whereas the quantum yield of Nd^{3+}:$NaGdF_4$ NPs was determined by comparing the emission spectrum with that of a standard reference sample with a defined quantum yield). Other important aspects that could account for different quantum yields is that they correspond to different core/shell nanocrystals and that they were fabricated in different laboratories and under different experimental conditions. This could influence the final Nd^{3+} emission quantum yield due to a different quality in the core/shell matching as well as to a different neodymium distribution. Indeed, the highest possible value should be that corresponding to the bulk core crystals. In general, at low neodymium contents, the quantum yield is expected to be close to 1, due to the large energy gap between the $^4F_{3/2}$ emitting state and the next lower $^4I_{15/2}$ state.[62] This is, indeed, what has been observed in this work, with quantum yield values for low Nd^{3+} contents close to 80%. Finally, the quantum yields reported here for Nd^{3+}:LaF_3 NPs can also be compared to those reported for the widely used Nd^{3+}:$NaYF_4$ NPs. For a 15 atom % Nd^{3+} content, the quantum yield of Nd^{3+}:$NaYF_4$ NPs has been reported to be 6%, which is more than 4 times lower than that obtained for Nd^{3+}:LaF_3 NPs.[63]

From the experimental data of Figure 2a, it is now possible to elucidate the influence of the Nd^{3+} content in the luminescence brightness of Nd^{3+}:LaF_3 NPs. Figure 2b shows the concentration dependence of the $[Nd^{3+}]\cdot\Phi_{lum}$ product. As expected, NP brightness does not follow a monotonous trend, revealing the existence of an optimum Nd^{3+} concentration close to 15 atom % (see the arrow in Figure 2b). Indeed, the existence of such optimum concentration has been experimentally corroborated. We have observed that the emitted intensity of Nd^{3+}:LaF_3 NP solutions (obtained under the same 808 nm excitation power and with the same NPs concentration) was maximum for the 15 atom % doped NPs (results not shown for the sake of brevity). As a consequence, for subtissue experiments, we will next focus our attention to 15 atom % doped Nd^{3+}:LaF_3 NPs.

Figure 3a schematically shows the experimental setup used for the determination of the tissue penetration depth of our Nd^{3+}:LaF_3 NPs. Briefly, 15 atom % Nd^{3+} doped NPs were dispersed in distilled water with

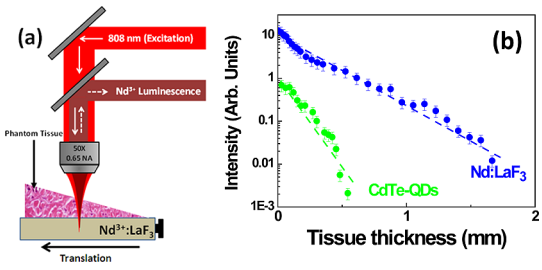

Figure 3. (a) Schematic diagram showing the experimental procedure to determine the penetration depth of Nd^{3+}:LaF_3 NPs. The phantom tissue used in these experiments (mimicking the *in vitro* human skin tissue) showed an extinction coefficient at 808 nm of 11 cm^{-1}. A triangular-shaped phantom tissue was placed between the focusing/collecting objective and the Nd^{3+}:LaF_3 NP solution. The actual tissue thickness between objective and Nd^{3+}:LaF_3 nanoparticles was continuously varied by moving the "*cuvette-plus-tissue*" system along a direction perpendicular to the laser beam propagation (as indicated by the arrow). (b) Intensity of the one-photon excited luminescence generated by Nd^{3+}:LaF_3 nanoparticles as a function of the tissue thickness. The excitation and emission wavelengths were 808 and 885 nm, respectively. Excitation power was 100 mW. For comparison, we have also included the intensity of the two-photon excited luminescence generated by CdTe-QDs as a function of the tissue thickness, using the same excitation intensity values as for the one-photon excitation case. Excitation and emission wavelengths in this former case were 920 and 780 nm, respectively. In this case, a 100 fs, 50 MHz Ti:sapphire mode-locked laser with an average power of 100 mW was used. Dots are experimental data, and dashed lines are the best fit to a linear relation (note the logarithmic scale).

a resulting NP concentration of 0.3% in mass. The colloidal solution was placed into a 200 μm deep microchannel (provided by Ibidi Inc.), and it was optically excited by a continuous wave 808 nm laser beam. This beam was focused into the microchannel by a 50× microscope objective (0.55 NA, leading to a spot size close to 2.5 μm). The same microscope objective was used for collection of the Nd^{3+} luminescence that, after passing through different filters and apertures, was analyzed by a high-resolution spectrometer (not shown in the figure for the sake of simplicity). A phantom tissue with a variable thickness was placed between the microchannel and the focusing objective. This setup allowed us to measure the NP luminescence as a function of the tissue thickness by simply translating the colloidal suspension. The phantom tissue used in this work consists of a scattering medium (such as agar) containing two main absorbing components (India ink and olive oil).[64−66] The ratio between the different components was adjusted to reproduce the main features of the extinction spectrum of an *in vitro* human skin tissue.[47] This is mainly given by the visible and infrared absorption bands of hemoglobin and water, respectively, superimposed on a background scattering coefficient close to 10 cm^{-1} in the 750−1000 nm range (see the extinction coefficient in Figure 1). Figure 3b shows the Nd^{3+}:LaF_3 NP emitted intensity (from the colloidal solution shown in Figure 1b) as a function of the phantom tissue thickness. Data correspond to the collected intensity at around 885 nm (corresponding to

one of the $^4F_{3/2} \rightarrow {}^4I_{9/2}$ transitions). Similar results were obtained when the luminescence intensity corresponding to $^4F_{3/2} \rightarrow {}^4I_{11/2}$ transition (at around 1060 nm) was analyzed. Indeed, this fact was expected because at both wavelengths the tissue shows similar extinction coefficients (see Figure 1). From data included in Figure 3b, it is evident that the use of Nd^{3+}:LaF_3 NPs allows for penetration depths into *in vitro* human skin tissues close to 2 mm. Of course, this penetration depth could be improved by increasing the excitation power as well as by improving the sensitivity of the detection systems. In any case, the penetration depth reported here is in the same order of magnitude as those achieved by using other rare-earth-doped NPs also emitting within the biological window.[67] In order to get a reliable comparison of the penetration depth reached by our NPs with that of the commercial quantum dots, we measured, in the same experimental conditions, the penetration depth of 8 nm CdTe-QDs. These luminescent nanoprobes have recently been proposed as promising NPs for subtissue imaging.[8] In this case, the Nd^{3+}:LaF_3 NP solution within the microchannel was replaced by a 8 nm CdTe-QD solution at the same concentration (0.3% in mass). Excitation of CdTe-QDs was achieved by using a 100 fs Ti:sapphire laser tuned to 920 nm so that the CdTe-QD emission at 780 nm was generated after a two-photon excitation process. The obtained CdTe-QD emitted intensity as a function of the tissue thickness is included in Figure 3b. As can be observed, much larger penetration depths are obtained by using Nd^{3+}:LaF_3 NPs instead of CdTe-QDs, although both systems work in the same spectral window and, hence, are affected by the same tissue extinction coefficient. We attribute this relevant difference to the different excitation mechanisms. When the excitation is performed *via* a multiphoton process, the overall luminescence efficiency is strongly dependent on the photon density at the excitation focus (it increases with the square of the excitation photon density).[68] At variance, in the case of one-photon excited luminescent systems (such as Nd^{3+}:LaF_3 NPs), this dependence is less critical; the luminescence increases linearly with the excitation photon density. When the excitation beam is focused into the tissue, the combination of tissue scattering, tissue absorption, beam distortions, and optical aberrations causes a fast decrease of the excitation intensity with the increasing tissue thickness. Because of the different excitation mechanisms, this in-depth excitation density reduction causes a more marked effect on the net excitation efficiency in multiphoton excited systems than in one-photon excited ones. This fact explains the larger penetration depths obtained for the one-photon excited Nd^{3+}:LaF_3 NPs. At this point, it should be noted that our conclusions are in reasonably good agreement with previous results reported by Gu *et al.*, who imaged a polymer bar placed in a turbid media by using both one- and two-photon excitation of the polymer fluorescence.[69] In this case, the authors found that the signal level obtained under two-photon excitation drops much faster than that under one-photon excitation, although image resolution was much higher in the former case (as expected for a nonlinear process). They attributed this to the fact that the penetration depth under two-photon excitation was limited by the strength of the two-photon absorption process.[69] Of course, the improvement achieved by using one-photon excitation in the penetration depth is gained at the expense of a loss in the final spatial resolution. Nevertheless, this loss of resolution could be partially compensated by using confocal microscopy. Finally, it should be noted that data included in Figure 3b reveal that under similar conditions (NP concentration, excitation intensity, exciting collecting optics, and so on) the emission intensity generated by the Nd^{3+}:LaF_3 NP colloidal solution has been found to be over 1 order of magnitude higher than that generated by the CdTe-QD colloidal solution. This larger efficiency is attributed to the fact that Nd^{3+}:LaF_3 NPs are excited by means of one-photon excitation (a down-conversion process), whereas for CdTe-QDs, a two-photon excitation process through virtual states is needed.[61]

Once the tissue penetration properties of Nd^{3+}:LaF_3 NPs have been demonstrated, the potential use of these NPs for subtissue thermal sensing requires an adequate knowledge of the thermal response of luminescence bands. For this purpose, the same experimental setup as that of subtissue measurement (Figure 3a) was used. Now the phantom tissue was removed, and the microchannel containing the Nd^{3+}:LaF_3 NP solution was placed on a 0.1 °C resolution temperature-controlled stage. Figure 4a shows the $^4F_{3/2} \rightarrow {}^4I_{9/2}$ emission spectra as obtained from the (15%) Nd^{3+}:LaF_3 NP colloidal solution at two different temperatures (10 and 60 °C). The first temperature-induced luminescence modification is observed in the most intense peak, at around 863 nm. The temperature increment from 10 up to 60 °C has red-shifted this emission line by more than 0.3 nm (see Figure 4b). Furthermore, this temperature-induced spectral shift has been found to be a linear effect, as can be observed in Figure 4d. As a matter of fact, the 863 nm peak shifts to longer wavelengths at an almost constant rate of 7×10^{-3} nm/°C. Therefore, from the spectral determination of the emission peak of Nd^{3+}:LaF_3 NPs, thermal sensing with a constant resolution over the biological range is possible. In order to get a better understanding of the physical mechanism causing this red shift of the 863 nm emission line, we have identified the Stark energy sublevels of both $^4F_{3/2}$ and $^4I_{9/2}$ manifold states that give place structure of the $^4F_{3/2} \rightarrow {}^4I_{9/2}$ emission spectrum (Figure 5a). For such purpose, we have deconvoluted this spectrum (obtained at 20 °C) into 10 Gaussian components (see Figure 5a), according to the same number of transitions which are expected to occur in relation to the crystal field energy components of the emitting ($^4F_{3/2}$) and ground ($^4I_{9/2}$) states. This has

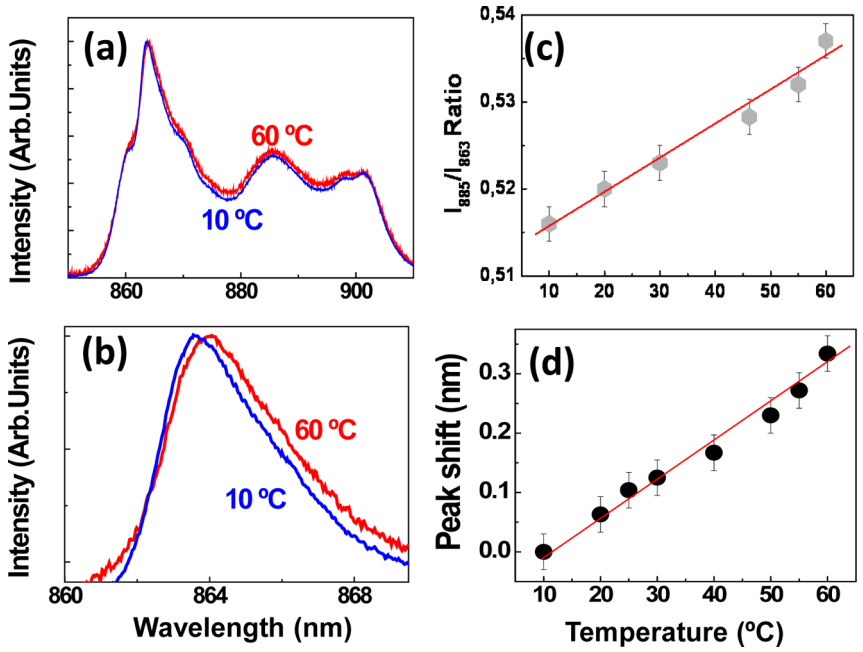

Figure 4. (a) Emission spectra of Nd^{3+}:LaF_3 nanoparticles as obtained at two different temperatures (10 and 60 °C and normalized at the maximum). (b) Details of the emission spectra of Nd^{3+}:LaF_3 nanoparticles around 864 nm as obtained at 10 and 60 °C. The temperature-induced spectral shift is evidenced. (c) Temperature variation of the ratio between the emitted intensities at 863 and 885 nm. Dots are experimental data, and the solid line is the best linear fit. (d) Temperature-induced spectral shift of the main emission line around 864 nm as a function of temperature. Dots are experimental data, and the solid line is the best linear fit.

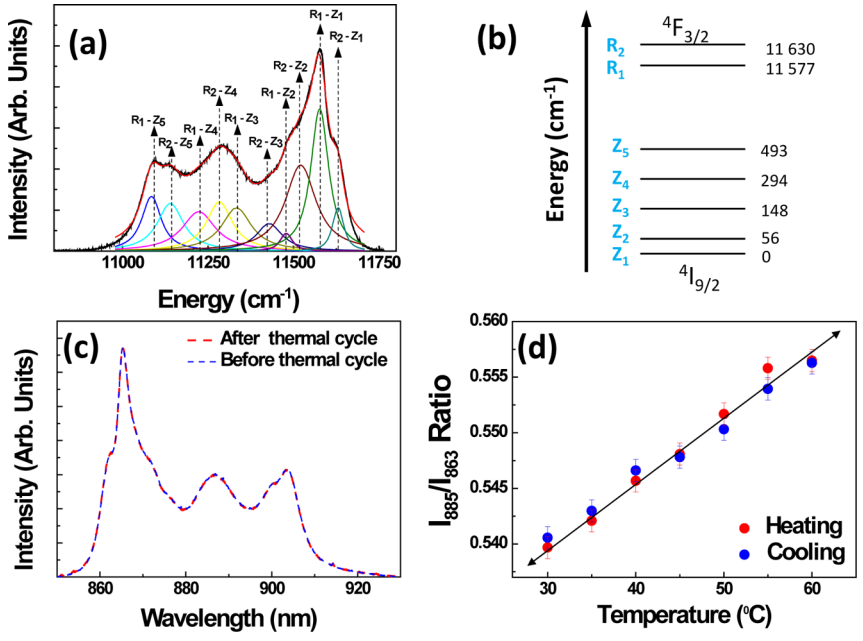

Figure 5. (a) Emission spectrum of Nd^{3+}:LaF_3 NPs as obtained at 20 °C and decomposed in the different emission lines constituting it. The emission lines have been properly labeled according to the energy level diagram shown in (b). (c) Emission spectra of Nd^{3+}:LaF_3 NPs at 30 °C as obtained before and after a thermal cycle from 30 °C up to 80 °C. No differences were observed, indicating the reversibility of the mechanisms. (d) Temperature variation of the ratio between the emitted intensities at 863 and 885 nm during the heating and cooling rate. No hysteresis is observed.

permitted us to construct a simplified energy level scheme (see Figure 5b) for the Nd^{3+} energy levels in the Nd^{3+}:LaF_3 NPs. This energy level has been found to be in excellent agreement with that previously reported for Nd^{3+} ions in bulk LaF_3 crystals. As can be observed, the emission peak at about 863 nm (around 11577 cm^{-1}) corresponds unequivocally to the $^4F_{3/2}(R_1) \rightarrow {}^4I_{9/2}(Z_1)$ transition. Thus, the observed spectral shift obeys to a temperature-induced modification of this transition. This temperature-induced red shift has been

systematically studied for bulk Nd^{3+}:LaF_3 crystals at low temperatures (below 200 K).[70] It was unequivocally associated with thermally induced strains in the Nd^{3+} environment that occur as a result of electron−phonon interaction. These strains are temperature-dependent through the correlated changes in the amplitude of the lattice vibrations that produce a substantial effect in the line position. In particular, for the $^4F_{3/2}(R_1) \rightarrow {}^4I_{9/2}(Z_1)$ transition, Nd^{3+}:LaF_3 varies linearly with temperature at a rate of about 0.14 cm^{-1} K^{-1}, similar to that experimentally observed for our Nd^{3+}:LaF_3 nanoparticles in the physiological temperature range (0.10 cm^{-1} K^{-1}), as estimated in Figure 4d). The temperature-induced spectral shift found here for the Nd^{3+}:LaF_3 NPs is much lower than others reported for fluorescent nanothermometers, such as QDs (on the order of 0.1 nm/°C),[26] but it is produced in a much narrower band; the bandwidth of the Nd^{3+} 863 nm emission is close to 3 nm, whereas the typical emission band of visible emitting QDs is on the order of several tens of nanometers. Therefore, the final contrast of the temperature-induced spectral shift (defined as the peak spectral shift divided by the bandwidth) is similar in both systems. The final thermal resolution achievable from the spectral determination of the 863 nm line obviously depends on the spectral resolution of the experimental setup and, in turn, on the signal level. In our experimental conditions, we estimated a net accuracy in the determination of the 863 nm peak position of 0.01 nm, leading to a thermal resolution close to 2 °C.

From a detailed analysis of data included in Figure 4a, it is observed that temperature also produces a modification of the intensity ratio between the different lines constituting the emission band. Indeed, we have found that a temperature increase of the NP from 10 up to 60 °C leads to an increase in the intensity ratio between the most intense peak (at around 863 nm) and the 885 nm peak close to 5% (*i.e.*, 0.1%/°C). As can be observed in Figure 4c, this ratio increment also follows a linear relation with temperature, so that thermal sensing based on this magnitude would lead to a constant resolution over the whole 10−60 °C physiological range. In this case, the final thermal resolution achievable depends on the signal-to-noise ratio of the emission spectra. In our experimental conditions, we have estimated a net uncertainty in the determination of the luminescence ratio close to ±0.2%, leading to a final thermal sensitivity close to ±2 °C. This can be compared to the thermal resolutions reported by using luminescent nanothermometers, usually below 4 °C.[23,24] Therefore, we conclude that Nd^{3+}:LaF_3 NPs are multiparameter luminescence thermal sensors, in the sense that thermal reading could be obtained by either the analysis of temperature-induced spectral shift of emission lines or ratiometric intensity measurements. The physical origin of the observed temperature-induced shape change (ratiometric change) can also be tentatively explained based on Figures 5a,b. As can be observed in Figure 5a, it is clear that many transitions generated from the R_2 ($^4F_{3/2}$) level contribute to the $^4F_{3/2} \rightarrow {}^4I_{9/2}$ fluorescence spectrum. This is because of a thermal population of the R_2 level from the R_1 lower energy level (see Figure 5b), so that both states belonging to the $^4F_{3/2}$ manifold are thermally coupled. The population of the $^4F_{3/2}(R_2)$ follows a Maxwell−Boltzmann temperature distribution. Therefore, the emission lines generated from the R_2 level increase with temperature, while those departing from the R_1 level decrease. Note from Figure 5a that at 863 nm (around 11 577 cm^{-1}) the emission is mostly dominated by the $R_1 \rightarrow Z_1$ transition, while at 885 nm (11 283 cm^{-1}), the emission is mostly dominated by the $R_2 \rightarrow Z_4$ transition. This explains the temperature-induced ratio change observed in Figure 4a. Similar effects have been observed for other Nd^{3+}-doped NPs and were explained in the same terms.[71]

The observed changes in the fluorescence spectrum of the Nd^{3+}:LaF_3 NPs that provide thermal sensitivity from the analysis of their fluorescence are all due to either modification in the energy level scheme or population redistributions within the different electronic states. Therefore, the observed changes in the fluorescence spectrum should be fully reversible. In order to confirm the reversibility of our Nd^{3+}:LaF_3 nanothermometers, we have measured the emission spectra at 30 °C as obtained before and after a heating cycle from 30 up to 70 °C. Results are included in Figure 5c. As can be observed, both spectra are identical, so that the thermal cycle has not caused any permanent modification in the luminescence spectrum of our Nd^{3+}:LaF_3 NPs. In addition, Figure 5d shows the temperature variation of the intensity ratio between the emission lines at 885 and 863 nm as obtained during the heating and cooling cycle. As can be observed, this a fully reversible process without any evidence of thermal hysteresis.

At this point, we have already demonstrated the potential use of Nd^{3+}:LaF_3 NPs for both subtissue luminescence imaging and luminescence-based thermal sensing. Combination of these two features would, in principle, allow for subtissue thermal sensing based on Nd^{3+}:LaF_3 NPs. In order to demonstrate this possibility, we took advantage of another outstanding property of our Nd^{3+}:LaF_3 NPs; they can be efficiently excited by 808 nm radiation, with this wavelength being the same required for plasmonic excitation of gold nanorods exhibiting a 100% heating efficiency and widely used in photothermal treatments.[48,72] This coincidence has been exploited in this work by the preparation of an aqueous solution containing both Nd^{3+}:LaF_3 NPs and GNRs at a concentration level of 0.3 and 0.01% in mass, respectively. The GNRs used in this work were provided by Plasmachem Inc. with nominal dimensions of 15 and 45 nm in diameter and length, respectively. The mixed suspension of Nd^{3+}:LaF_3

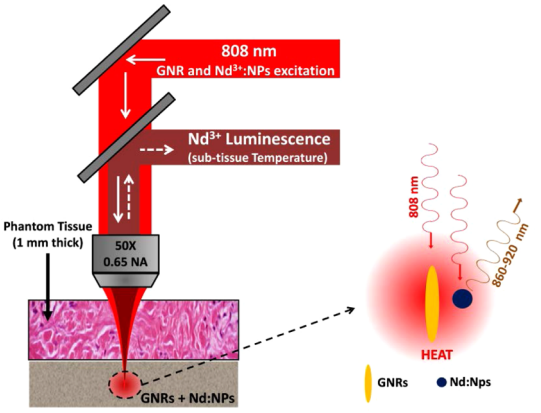

Figure 6. Schematic representation of the experimental setup used for single-beam sub-tissue-controlled hyperthermia. A 808 nm laser beam is focused into an aqueous solution containing GNRs (nanoheaters) and Nd^{3+}:LaF_3 nanoparticless (nanothermometers). The solution was placed under a 1 mm thick phantom tissue. The luminescence of Nd^{3+}:LaF_3 nanoparticles was collected by using the same objective, and the subtissue temperature was extracted from its spectral analysis. Diagram at the right reflects the fact that both GNRs and Nd^{3+}:LaF_3 NPs were simultaneously excited by the 808 nm radiation.

NPs and GNRs showed an extinction coefficient close to 10 cm^{-1} at 808 nm (plasmon resonance wavelength of GNR) and displayed a stable colloidal behavior with no evidence of precipitation for weeks. The mixed solution was injected into a 100 μm height microchannel that was placed under a 1 mm thick phantom tissue mimicking the *in vitro* human skin tissue, as it is schematically illustrated in Figure 6. The continuous wave 808 nm laser radiation of a single-mode fiber-coupled diode was focused through the tissue into the mixed solution by using a long working distance 50× microscope objective with a numerical aperture of 0.65. Laser power (measured at the back aperture of the microscope objective) was varied between 30 and 85 mW. The luminescence generated by the Nd^{3+}:LaF_3 NPs was collected by the same microscope objective, and after passing through several filters and objectives, it was spectrally analyzed by a high-resolution spectrometer. The 808 nm radiation reaching the mixed solution simultaneously activates two different processes, as illustrated in Figure 6. On the one hand, the 808 nm laser radiation excites the collective motion of surface electrons of GNRs (*i.e.*, it activates the plasmonic resonance), whose subsequent relaxation leads to a local heating of the solution. On the other hand, the 808 nm photons also activate the luminescence of the Nd^{3+}:LaF_3 NPs located at the laser focal volume. The spectral properties of this luminescence would be determined by the actual on-focus temperature. Thus, an adequate analysis of the luminescence generated by the mixed solution would, in principle, determine the temperature associated with laser-induced plasmonic subtissue hyperthermia. Results included in Figure 7 demonstrate this possibility.

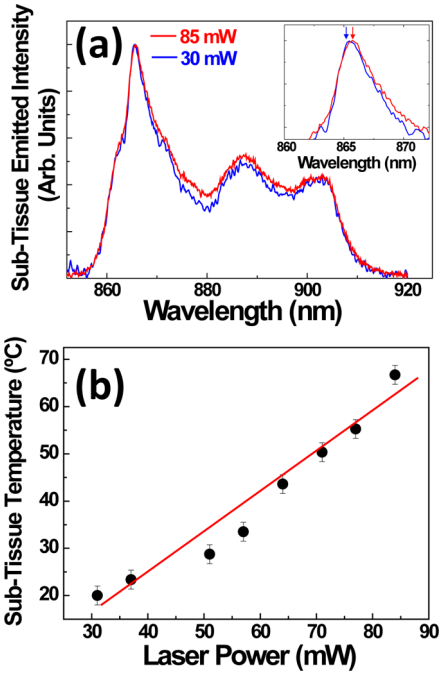

Figure 7. (a) Subtissue normalized emission spectra generated by Nd^{3+}:LaF_3 nanoparticles as obtained for two different 808 nm laser powers (30 and 85 mW). For the sake of clarity, both spectra were normalized to their maximum intensities. Before normalization, the emitted intensity obtained under 30 mW excitation power was almost 3 times lower than that obtained under an excitation power of 85 mW. Inset shows a detail of the 863 nm emission peak revealing the red shift. (b) Subtissue temperature as a function of the 808 nm laser power calculated from the ratiometric analysis of the subtissue fluorescence spectra. Dots are experimental data, and the dashed line is the best linear fit.

Figure 7a shows the subtissue luminescence spectra generated from the Nd^{3+}:LaF_3 NPs as obtained for two different 808 nm laser powers. It is evident that the increment in the 808 nm laser power produces changes in the fluorescence features of our nanothermometers. The decrease in the intensity ratio between the 863 and 885 nm lines clearly shows the presence of a relevant subtissue local heating as a consequence of the plasmonic excitation of GNRs. It should be noted that in these experiments, and due to the presence of the phantom tissue, the emission spectra were found to be noisier than those obtained during the thermal calibration procedure. In these conditions, the temperature-induced red shift of the 863 nm emission line is also observed (see inset in Figure 7a), but the determination of its magnitude is less accurate when decreasing the temperature resolution from its analysis. Therefore, a more accurate determination of the subtissue laser-induced temperature increment is in this case obtained from the analysis of the variation in the ratio between emission intensities (by using the calibration curve included in Figure 4c). Results are shown in Figure 7b, which includes the subtissue temperature as a function of the 808 nm laser power, reflecting an almost linear behavior. Subtissue temperatures as large as

70 °C have been achieved. This temperature reflects the large heating efficiency of GNRs and is enough by far to activate hyperthermia treatments. Thus, data included in Figure 7b constitute the first evidence of the possibility of a sub-tissue-controlled laser-induced hyperthermia process. In fact, on the basis of this novel approach, the actual subtissue temperature can be monitored in real time, allowing for complete control over the subtissue temperature. Note that this sub-tissue-controlled hyperthermia would be achieved by using a single laser beam. Again, this is based on the fact that both the nanoheaters (GNRs) and luminescent nanothermometers (Nd^{3+}:LaF_3 NPs) used in the process are excited by the same laser radiation, which we view as a great practical advantage. This is at variance with recent proposals for real-time controlled hyperthermia in which two different beams were employed: one for laser excitation of GNRs and a second one for luminescence activation of the luminescent nanothermometers.[72]

CONCLUSIONS

In summary, we have performed a systematic investigation of the luminescence properties of Nd^{3+}-doped LaF_3 (core) nanoparticles shielded by an undoped LaF_3 shell. Under infrared (808 nm) optical excitation, these nanoparticles show very intense Nd^{3+} emission bands at around 885 and 1060 nm, both overlapping with the transparency windows of human tissues, that is, lying in the so-called biological window. Thermal lens spectroscopy has been applied to determine the luminescence quantum yield of these core−shell Nd^{3+}:LaF_3 nanoparticles. Luminescence quantum yields in excess of 80% have been found for low (<1 atom %) neodymium doping levels, due to the absence of relevant energy transfer and cross-relaxation processes as well as the minimization of surface quenching channels. On the other hand, for large neodymium contents (>20 atom %), energy transfer between neodymium ions increases the nonradiative decay rates, thus leading to low (below 25%) emission quantum yields. It has been found that for neodymium contents close to 15 atom % the luminescence brightness of the Nd^{3+}:LaF_3 nanoparticles is optimized. Under these optimum doping conditions, subtissue penetration lengths achievable with one-photon excited Nd^{3+}:LaF_3/LaF_3 nanoparticles have been found to be close to 2 mm. This is significantly larger than the penetration length achieved by two-photon excited/infrared emitting CdTe quantum dots.

In addition to their ability for subtissue penetration, Nd^{3+}:LaF_3 nanoparticles have also been found to display a remarkable luminescence thermal sensitivity with a value of ±2 °C. Temperature variations within the biological range have been found to cause linear modifications in both the spectral position of emission lines as well as on the relative intensities of the different lines. Combination of these two outstanding properties, large penetration depths into human tissues and remarkable thermal sensitivity of fluorescence bands, has been exploited for the achievement of subtissue thermal sensing based on Nd^{3+}:LaF_3 nanoparticles. As a matter of fact, we have demonstrated that, when combined with adequate gold nanorods, Nd^{3+}:LaF_3 nanoparticles can be potentially used as reference nanothermometers in single-beam subtissue hyperthermia treatments.

We are firmly convinced that results included in this work would stimulate the use of neodymium-doped nanoparticles for subtissue remote thermal sensing with numerous applications in a large variety of fields including early diagnosis and controlled thermal treatments.

METHODS

Synthesis. The Nd^{3+}-doped LaF_3 core/shell nanoparticles used in this work were prepared by the co-precipitation technique in aqueous solution in the presence of citrate ions. Around 3 g of citric acid was dissolved in 35 mL of water and neutralized with NH_4−OH until the pH reached around 6, and this solution was then heated to 75 °C. $La(NO_3)_3 \cdot 6H_2O$ and $Nd(NO_3)_3 \cdot 6H_2O$ were dissolved in 3 mL of methanol and added to this followed by the dropwise addition of 3 mL of water containing 0.266 g of NaF. After 10 min, 3 mL of a methanolic solution containing 0.6 g of $La(NO_3)_3 \cdot 6H_2O$ was added dropwise to the reaction mixture while stirring for the formation of shell around the core particles. The reaction was allowed to continue for 2 h, and finally, the nanoparticles were precipitated by the addition of excess ethanol to the reaction mixture. They were collected by centrifuge and dried for 24 h.

Spectroscopic Measurements. For fluorescence measurements, the Nd^{3+}:LaF_3 colloidal solutions under study in this work were optically excited with a single-mode fiber-coupled 808 nm laser diode providing a maximum power of 100 mW. The 808 nm laser beam was focused into the colloidal suspension by using a 50× long working distance microscope objective (NA 0.55). The infrared fluorescence was collected using the same microscope objective and, after passing through several filters and apertures, was spectrally analyzed by a high-resolution spectrometer. For thermal sensitivity experiments, the solution was mounted on a heating microscope stage with temperature control from 25 to 65 °C with a resolution of 1 °C.

Optical Penetration in Phantom Tissues. The phantom tissue used throughout this work was fabricated by mixing a scattering medium (agar) with several absorbing components (blue India ink, olive oil, and water) so that the optical properties of *in vitro* human skin were mimicked. The use of agarose (one of the main components of agar) as scattering medium in phantom tissues was first reported by Cubeddu *et al.*[66] Hemoglobin and melanin are the main components responsible for the absorption in the visible and the ultraviolet, as reported by Kobayashi *et al.*[65] A certain amount (0.36 g) of microbiological agar powder was first dissolved in distilled water to get a solution with around 1% of the total volume. Then appropriate amounts of olive oil and blue India ink were added to the mixture. The optimal percentages to mimic the absorption of *in vitro* human skin were 0.50% (200 μL) of blue India ink and 0.32% (128 μL) of olive oil as added directly to the mentioned agar/water solution. For the comparative studies of tissue penetration with our Nd^{3+}:LaF_3 nanocrystals/water solution, we used an aqueous suspension of CdTe

quantum dots provided by Plasmachem Inc. (7.8 nm in diameter). This solution was excited by a mode-locked Ti:sapphire laser (Tsunami, Spectra Physics) tuned to 920 nm and providing 100 fs laser pulses at a repetition rate of 50 MHz. Average laser power was 100 mW (same power used for the determination of the penetration depth of Nd^{3+}:LaF_3 NPs). The 920 nm laser beam was focused into the colloidal suspension using a 50× long working distance microscope objective (NA 0.55). The infrared fluorescence was collected using the same microscope objective and, after passing through several filters and apertures, was spectrally analyzed by a high-resolution spectrometer.

Single-Beam Subtissue Hyperthermia. The gold nanorods used in this work were provided by NanoPartz Inc. They were bare gold nanorods with a mean diameter of 15 nm and a mean length of 45 nm. The longitudinal plasmon resonance was centered at 808 nm.

Conflict of Interest: The authors declare no competing financial interest.

Acknowledgment. This work has been financed by NSERC (the National Science and Engineering Council of Canada) by the Universidad Autónoma de Madrid and Comunidad Autónoma de Madrid (Projects CCG087-UAM/MAT-4434 and S2009/MAT-1756, PHAMA), by the Spanish Ministerio de Educacion y Ciencia (MAT2010-16161), and by PRONEX/FAPEAL (Project 2009-09-006), FINEP (Financiadora de Estudos e Projetos), CNPq (Conselho Nacional de Desenvolvimento Científico e Tecnológico through Grant INCT NANO(BIO)SIMES), and CAPES (Coordenadoria de Aperfeiçoamento de Pessoal de Ensino Superior) Brazilian Agencies. The research of U.R. is supported by a graduate studentship from CAPES and actually by a PDSE-CAPES program developed in the Universidad Autonoma de Madrid, Spain. A. Benayas gratefully acknowledges Le Fonds de recherche du Québec Nature et technologies (FRQNT) for the Postdoctoral Fellowship granted to him through "Programme de Bourses d' Excellence".

REFERENCES AND NOTES

1. Altinoglu, E. I.; Russin, T. J.; Kaiser, J. M.; Barth, B. M.; Eklund, P. C.; Kester, M.; Adair, J. H. Near-Infrared Emitting Fluorophore-Doped Calcium Phosphate Nanoparticles for *In Vivo* Imaging of Human Breast Cancer. *ACS Nano* **2008**, *2*, 2075–2084.
2. Jiang, S.; Zhang, Y.; Lim, K. M.; Sim, E. K. W.; Ye, L. Visible Upconversion Nanoparticles for Fluorescent Labeling and Targeted Delivery of siRNA. *Nanotechnology* **2009**, *20*, 155101.
3. Foy, S. P.; Manthe, R. L.; Foy, S. T.; Dimitrijevic, S.; Krishnamurthy, N.; Labhasetwar, V. Optical Imaging and Magnetic Field Targeting of Magnetic Nanoparticles in Tumors. *ACS Nano* **2010**, *4*, 5217–5224.
4. Xu, C. T.; Axelsson, J.; Andersson-Engels, S. Fluorescence Diffuse Optical Tomography Using Upconverting Nanoparticles. *Appl. Phys. Lett.* **2009**, *94*, 251107.
5. Naccache, R.; Rodíguez, E. M.; Bogdan, N.; Sanz-Rodríguez, F.; de la Cruz, M. C. I.; de la Fuente, A. J.; Vetrone, F.; Jaque, D.; García Solé, J.; Capobianco, J. A. High Resolution Imaging of Cancers Using Lanthanide Ion-Doped Upconverting Nanocrystals. *Cancers* **2012**, *4*, 1067–1105.
6. Ntziachristos, V.; Ripoll, J.; Wang, L. H. V.; Weissleder, R. Looking and Listening to Light: The Evolution of Whole-Body Photonic Imaging. *Nat. Biotechnol.* **2005**, *23*, 313–320.
7. Michalet, X.; Pinaud, F. F.; Bentolila, L. A.; Tsay, J. M.; Doose, S.; Li, J. J.; Sundaresan, G.; Wu, A. M.; Gambhir, S. S.; Weiss, S. Quantum Dots for Live Cells, *In Vivo* Imaging, and Diagnostics. *Science* **2005**, *307*, 538–544.
8. Maestro, L. M.; Ramírez-Hernandes, J. E.; Bogdan, N.; Capobianco, J. A.; Vetrone, F.; García Solé, J.; Jaque, D. Deep Tissue Bio-imaging Using Two-Photon Excited CdTe Fluorescent Quantum Dots Working within the Biological Window. *Nanoscale* **2012**, *4*, 298–302.
9. Nagarajan, S.; Zhang, Y. Upconversion Fluorescent Nanoparticles as a Potential Tool for In-Depth Imaging. *Nanotechnology* **2011**, *22*, 395101.
10. Medintz, I. L.; Uyeda, H. T.; Goldman, E. R.; Mattoussi, H. Quantum Dot Bioconjugates for Imaging, Labelling and Sensing. *Nat. Mater.* **2005**, *4*, 435–446.
11. Vetrone, F.; Naccache, R.; de la Fuente, A. J.; Sanz-Rodriguez, F.; Blazquez-Castro, A.; Rodriguez, E. M.; Jaque, D.; García Solé, J.; Capobianco, J. A. Intracellular Imaging of HeLa Cells by Non-functionalized $NaYF_4$:Er^{+3},Yb^{+3} Upconverting Nanoparticles. *Nanoscale* **2010**, *2*, 495–498.
12. Idris, N. M.; Li, Z. Q.; Ye, L.; Sim, E. K. W.; Mahendran, R.; Ho, P. C. L.; Zhang, Y. Tracking Transplanted Cells in Live Animal Using Upconversion Fluorescent Nanoparticles. *Biomaterials* **2009**, *30*, 5104–5113.
13. Chen, Y.; Yang, L.; Feng, C.; Wen, L.-P. Nano Neodymium Oxide Induces Massive Vacuolization and Autophagic Cell Death in Non-small Cell Lung Cancer NCI-H460 Cells. *Biochem. Biophys. Res. Commun.* **2005**, *337*, 52–60.
14. Chatteriee, D. K.; Rufalhah, A. J.; Zhang, Y. Upconversion Fluorescence Imaging of Cells and Small Animals Using Lanthanide Doped Nanocrystals. *Biomaterials* **2008**, *29*, 937–943.
15. Zhou, J.; Sun, Y.; Du, X. X.; Xiong, L. Q.; Hu, H.; Li, F. Y. Dual-Modality *In Vivo* Imaging Using Rare-Earth Nanocrystals with Near-Infrared to Near-Infrared (NIR-to-NIR) Upconversion Luminescence and Magnetic Resonance Properties. *Biomaterials* **2010**, *31*, 3287–3295.
16. Nyk, M.; Kumar, R.; Ohulchanskyy, T. Y.; Bergey, E. J.; Prasad, P. N. High Contrast *In Vitro* and *In Vivo* Photoluminescence Bioimaging Using Near Infrared to Near Infrared Up-Conversion in Tm^{+3} and Yb^{+3} Doped Fluoride Nanophosphors. *Nano Lett.* **2008**, *8*, 3834–3838.
17. Chen, G.; Ohulchanskyy, T. Y.; Liu, S.; Law, W.-C.; Wu, F.; Swihart, M. T.; Agren, H.; Prasad, P. N. Core/Shell $NaGdF_4$:Nd^{+3}/$NaGdF_4$ Nanocrystals with Efficient Near-Infrared to Near-Infrared Downconversion Photoluminescence for Bioimaging Applications. *ACS Nano* **2012**, *6*, 2969–2977.
18. Krasnovsky, J. A. A.; Drozdova, N. N.; Ivanov, A. V.; Ambartsumian, R. V. Activation of Molecular Oxygen by Infrared Laser Radiation in Pigment-Free Aerobic Systems. *Biochemistry (Moscow)* **2003**, *68*, 1178–1182.
19. Nathan, R. A.; Adelman, A. H. Photosensitized Generation of Singlet Molecular Oxygen with Near-Infrared Radiation. *J. Chem. Soc., Chem. Commun.* **1974**, 674–675.
20. Cao, T.; Yang, Y.; Gao, Y.; Zhou, J.; Li, Z.; Li, F. High-Quality Water-Soluble and Surface-Functionalized Upconversion Nanocrystals as Luminescent Probes for Bioimaging. *Biomaterials* **2011**, *32*, 2959–2968.
21. Wang, F.; Zhang, Y.; Fan, X.; Wang, M. One-Pot Synthesis of Chitosan/LaF_3:Eu^{3+} Nanocrystals for Bio-applications. *Nanotechnology* **2006**, *17*, 1527–1532.
22. Xie, M.-Y.; Yu, L.; He, H.; Yu, X.-F. Synthesis of Highly Fluorescent LaF_3:Ln^{3+}/LaF_3 Core/Shell Nanocrystals by a Surfactant-Free Aqueous Solution Route. *J. Solid State Chem.* **2009**, *182*, 597–601.
23. Brites, C. D. S.; Lima, P. P.; Silva, N. J. O.; Millán, A.; Amaral, V. S.; Palacio, F.; Carlos, L. D. Thermometry at the Nanoscale. *Nanoscale* **2012**, *4*, 4799–4829.
24. Jaque, D.; Vetrone, F. Luminescence Nanothermometry. *Nanoscale* **2012**, *4*, 4301–4326.
25. Vetrone, F.; Naccache, R.; Zamarron, A.; de la Fuente, A. J.; Sanz-Rodriguez, F.; Maestro, L. M.; Rodriguez, E. M.; Jaque, D.; García Solé, J.; Capobianco, J. A. Temperature Sensing Using Fluorescent Nanothermometers. *ACS Nano* **2010**, *4*, 3254–3258.
26. Maestro, L. M.; Rodriguez, E. M.; Cruz, M. C. I.; Juarranz, A.; Naccache, R.; Vetrone, F.; Jaque, D.; Capobianco, J. A.; García Solé, J. CdSe Quantum Dots for Two-Photon Fluorescence Thermal Imaging. *Nano Lett.* **2010**, *10*, 5109–5115.
27. Engeser, M.; Fabbrizzi, L.; Licchelli, M.; Sacch, D. A Fluorescent Molecular Thermometer Based on the Nickel(II) High-Spin/Low-Spin Interconversion. *Chem. Commun.* **1999**, *13*, 1191–1192.
28. Bednarkiewicz, A.; Wawrzynczyk, D.; Nyk, M.; Strek, W. Optically Stimulated Heating Using Nd^{3+} Noped $NaYF_4$ Colloidal Near Infrared Nanophosphors. *Appl. Phys. B: Lasers Opt.* **2011**, *103*, 847–852.

29. Zohar, O.; Ikeda, M.; Shinagawa, H.; Inoue, H.; Nakamura, H.; Elbaum, D.; Alkon, D. L.; Yoshioka, T. Thermal Imaging of Receptor-Activated Heat Production in Single Cells. *Biophys. J.* **1998**, *74*, 82–89.
30. Suzuki, M.; Tseeb, V.; Oyama, K.; Ishiwata, S. Microscopic Detection of Thermogenesis in a Single HeLa Cell. *Biophys. J.* **2007**, *92*, L46–L48.
31. Tardieu, F.; Reymond, M.; Hamard, P.; Grainer, C.; Muller, B. Spatial Distributions of Expansion Rate, Cell Division Rate and Cell Size in Maize Leaves: A Synthesis of the Effects of Soil Water Status, Evaporative Demand and Temperature. *J. Exp. Bot.* **2000**, *51*, 1505–1514.
32. Sanchez, B. M.; Lesch, M.; Brammer, D.; Bove, S. E.; Thiel, M.; Kilgore, K. S. Use of a Portable Thermal Imaging Unit as a Rapid, Quantitative Method of Evaluating Inflammation and Experimental Arthritis. *J. Pharmacol. Toxicol. Methods* **2008**, *57*, 169–175.
33. Stark, A. M.; Way, S. The Use of Thermovision in the Detection of Early Breast Cancer. *Cancer* **1974**, *33*, 1664–1670.
34. Matsuda, H.; Sugimachi, K.; Kuwano, H. Hyperthermia, Tissue Microcirculation, and Temporarily Increased Thermosensitivity in VX2 Carcinoma in Rabbit Liver. *Cancer Res.* **1989**, *49*, 2777–2782.
35. Huff, T. B.; Tong, L.; Zhao, Y.; Hansen, M. N.; Cheng, J.-X.; Wei, A. Hyperthermic Effects of Golds Nanorods on Tumor Cells. *Nanomedicine* **2007**, *2*, 125–132.
36. Chung, S. H.; Mehta, R.; Tromberg, B. J.; Yodh, A. G. Noninvasive Measurement of Deep Tissue Temperature Changes Caused by Apoptosis during Breast Cancer Neoadjuvant Chemotherapy: A Case Study. *J. Innovative Opt. Health Sci.* **2011**, *4*, 361–372.
37. Weissleder, R. A Clear Vision for *In Vivo* Imaging. *Nat. Biotechnol.* **2001**, *19*, 316–317.
38. Bovero, E.; Veggel, F. C. J. M. Conformational Characterization of Eu^{3+}-Doped LaF_3 Core−Shell Nanoparticles through Luminescence Anisotropy Studies. *J. Phys. Chem. C* **2007**, *111*, 4529–4534.
39. Sudarsan, V.; Sivakumar, S.; Veggel, F. C. J. M. General and Convenient Method for Making Highly Luminescent Sol−Gel Derived Silica and Alumina Films by Using LaF_3 Nanoparticles Doped with Lanthanide Ions (Er^{3+}, Nd^{3+}, and Ho^{3+}). *Chem. Mater.* **2005**, *17*, 4736–4742.
40. Diamente, P. R.; Veggel, F. C. J. M. Water-Soluble Ln^{+3}-Doped LaF_3 Nanoparticles: Retention of Strong Luminescence and Potential as Biolabels. *J. Fluoresc.* **2005**, *15*, 543–551.
41. Cui, X.; Shen, J.; Gao, C.; Cui, K.; Hou, C.; Wei, W.; Peng, B. Luminescent Properties of Nd^{3+}-Doped LaF_3 Core/Shell Nanoparticles wth Enhanced Near Infrared (NIR) Emission. *Chem. Phys. Lett.* **2010**, *494*, 60–63.
42. Dekker, R.; Klunder, D. J. W.; Borreman, A.; Diemeer, M. B. J.; Wörhoff, K. Stimulated Emission and Optical Gain in LaF_3: Nd Nanoparticle-Doped Polymer-Based Waveguides. *Appl. Phys. Lett.* **2004**, *85*, 6104–6106.
43. Stouwdam, J. W.; Veggel, F. C. J. M. Near-Infrared Emission of Redispersible Er^{3+}, Nd^{3+}, and Ho^{3+} Doped LaF_3 Nanoparticles. *Nano Lett.* **2002**, *2*, 733–737.
44. Bashkatov, A. N.; Genina, E. A.; Kochubey, V. I.; Tuchin, V. V. Optical Properties of Human Skin, Subcutaneous and Mucous Tissues in the Wavelength Range from 400 to 2000 nm. *J. Phys. D: Appl. Phys.* **2005**, *38*, 2543–2555.
45. Frangioni, J. V. *In Vivo* Near-Infrared Fluorescence Imaging. *Curr. Opin. Chem. Biol.* **2003**, *7*, 626–634.
46. Marquez, G.; Wang, L. H. V.; Lin, S. P.; Schwartz, J. A.; Thomsen, S. L. Anisotropy in the Absorption and Scattering Spectra of Chicken Breast Tissue. *Appl. Opt.* **1998**, *37*, 798–804.
47. Welsher, K.; Sherlock, S. P.; Dai, H. Deep-Tissue Anatomical Imaging of Mice Using Carbon Nanotube Fluorophores in the Second Near-Infrared Window. *Proc. Natl. Acad. Sci. U.S.A.* **2011**, *108*, 8943–8948.
48. Maestro, L. M.; Haro-Gonzáles, P.; Coello, J. G.; Jaque, D. Absorption Efficiency of Gold Nanorods Determined by Quantum Dot Fluorescence Thermometry. *Appl. Phys. Lett.* **2012**, *100*, 201110.
49. Powell, R. C. *Physics of Solid-State Laser Materials*; Springer-Verlag: New York, 1998.
50. Campbell, J. H.; Suratwala, T. I. Nd-Doped Phosphate Glasses for High-Energy/High-Peak-Power Lasers. *J. Non-Cryst. Solids* **2000**, *318*, 318–341.
51. Santos, D. R. S.; Santos, C. N.; Camargo, A. S. S.; Silva, W. F.; Santos, W. Q.; Vermelho, M. V. D.; Astrath, N. G. C.; Malacarne, L. C.; Li, M. S.; Hernandes, A. C.; *et al.* Thermo-optical Characteristics and Concentration Quenching Effects in Nd^{3+} Doped Yttrium Calcium Borate Glasses. *J. Chem. Phys.* **2011**, *134*, 124503.
52. Lupei, V.; Lupei, A.; Georgescu, S.; Taira, T.; Sato, Y.; Ikesue, A. The Effect of Nd Concentration on the Spectroscopic and Emission Decay Properties of Highly Doped Nd:YAG Ceramics. *Phys. Rev. B: Condens. Matter Mater. Phys.* **2001**, *64*, 092102.
53. Shen, J.; Lowe, R. D.; Snook, R. D. A Model for CW Laser Induced Mode-Mismatched Dual-Beam Thermal Lens Spectrometry. *Chem. Phys.* **1992**, *165*, 385–396.
54. Baesso, M. L.; Shen, J.; Snook, R. D. Time-Resolved Thermal Lens Measurement of Thermal Diffusivity of Soda−Lime Glass. *Chem. Phys. Lett.* **1992**, *197*, 255–258.
55. Jacinto, C.; Messias, D. N.; Andrade, A. A.; Lima, S. M.; Baesso, M. L.; Catunda, T. Thermal Lens and Z-Scan Measurements: Thermal and Optical Properties of Laser Glasses. *J. Non-Cryst. Solids* **2006**, *352*, 3582–3597.
56. Maestro, L. M.; Jacinto, C.; Rocha, U.; Cruz, M. C. I.; Sanz-Rodriguez, F. Optimum Quantum Dot Size for Highly Efficient Fluorescence Bioimaging. *J. Appl. Phys.* **2012**, *11*, 023513.
57. Cruz, R. A.; Pilla, V.; Catunda, T. Quantum Yield Excitation Spectrum (UV−Visible) of CdSe/ZnS Core−Shell Quantum Dots by Thermal Lens Spectrometry. *J. Appl. Phys.* **2010**, *107*, 083504.
58. Henderson, B.; Imbusch, G. F. *Optical Spectroscopy of Inorganic Solids*; Oxford Science Publications: New York, 2006.
59. Sun, W.; Cui, X.; Wang, Z.; Wei, W.; Peng, B. Luminescence Properties of Nd^{3+}-Doped LaF_3 Nanocrystals with a Long Lifetime in Organic Solvents. *J. Mater. Chem.* **2012**, *22*, 6990–6993.
60. Kumar, G. A.; Chen, C. W.; Ballato, J.; Riman, R. E. Optical Characterization of Infrared Emitting Rare-Earth-Doped Fluoride Nanocrystals and Their Transparent Nanocomposites. *Chem. Mater.* **2007**, *19*, 1523–1528.
61. Maestro, L. M.; Rodriguez, E. M.; Vetrone, F.; Naccache, R.; Ramirez, H. L.; Jaque, D.; Capobianco, J. A.; García Solé, J. Nanoparticle for Highly Efficienty Multiphoton Fluorescence Bioimaging. *Opt. Express* **2010**, *18*, 23544–23553.
62. García Solé, J.; Baussá, L. E.; Jaque, D. *An Introduction to the Optical Spectroscopy of Inorganic Solids*; John Wiley & Sons: New York, 2005.
63. Bednarkiewicz, A.; Wawrzynczyk, D.; Nyk, M.; Strek, W. Synthesis and Spectral Properties of Colloidal Nd^{3+} Doped $NaYF_4$ Nanocrystals. *Opt. Mater.* **2011**, *33*, 1481–1486.
64. Madsen, S. J.; Patterson, M. S.; Wilson, B. C. The Use of India Ink as an Optical Absorber in Tissue-Simulating Phantoms. *Phys. Med. Biol.* **1992**, *37*, 985–993.
65. Kobayashi, M.; Ito, Y.; Sakauchi, N.; Oda, I.; Konishi, I.; Tsunazawa, Y. Analysis of Nonlinear Relation for Skin Hemoglobin Imaging. *Opt. Express* **2001**, *9*, 802–812.
66. Cubeddu, R.; Pifferi, A.; Taroni, P.; Torricelli, A.; Valentini, G. Time-Resolved Imaging on a Realistic Tissue Phantom: $\mu s'$ and μa Images *versus* Time-Integrated Images. *Appl. Opt.* **1996**, *35*, 4533–4540.
67. Dong, N. N.; Pedroni, M.; Piccinelli, F.; Conti, G.; Sbarbati, A.; Ramírez-Hernández, J. E.; Maestro, L. M.; Cruz, M. C. I. I.; Sanz-Rodriguez, F.; Juarranz, A.; *et al.* NIR-to-NIR Two-Photon Excited CaF_2: Tm^{+3},Yb^{+3} Nanoparticles: Multifunctional Nanoprobes for Highly Penetrating Fluorescence Bio-imaging. *ACS Nano* **2011**, *5*, 8665–8671.
68. Helmchen, F.; Denk, W. Deep Tissue Two-Photon Microscopy. *Nat. Methods* **2005**, *2*, 932–940.
69. Gu, M.; Gan, X.; Kisteman, A.; Xu, M. G. Comparison of Penetration Depth between Two-Photon Excitation and

Single-Photon Excitation in Imaging through Turbid Tissue Media. *Appl. Phys. Lett.* **2000**, *77*, 1551–1553.
70. Johnson, S. A.; Freire, H. G.; Schawlow, A. L.; Yen, W. M. Thermal Shifts in the Energy Levels of LaF_3:Nd^3. *J. Opt. Soc. Am.* **1967**, *57*, 734–737.
71. Wawrzynczyk, D.; Bednarkiewicz, A.; Nyk, M.; Strek, W.; Samoc, M. Neodymium(III) Doped Fluoride Nanoparticles as Non-contact Optical Temperature Sensors. *Nanoscale* **2012**, *4*, 6959–6961.
72. Maestro, L. M.; Haro, P.; Iglesias, M. C.; Sanz, F.; García Solé, J.; Jaque, D. Fluorescent Nano-thermometers Provide Controlled Plasmonic Mediated Intracellular Hyperthermia. *Nanomedicine* **2013**, 10.2217/nnm.12.122.